

This discussion paper is/has been under review for the journal *Climate of the Past* (CP).  
Please refer to the corresponding final paper in CP if available.

# A model-data comparison for a multi-model ensemble of early Eocene atmosphere-ocean simulations: EoMIP

D. J. Lunt<sup>1</sup>, T. Dunkley Jones<sup>2</sup>, M. Heinemann<sup>3</sup>, M. Huber<sup>4</sup>, A. LeGrande<sup>5</sup>,  
A. Winguth<sup>6</sup>, C. Loptson<sup>1</sup>, J. Marotzke<sup>7</sup>, J. Tindall<sup>8</sup>, P. Valdes<sup>1</sup>, and C. Winguth<sup>6</sup>

<sup>1</sup>School of Geographical Sciences, University of Bristol, UK

<sup>2</sup>Department of Earth Science and Engineering, Imperial College London, UK

<sup>3</sup>International Pacific Research Center, University of Hawaii, USA

<sup>4</sup>Department of Earth and Atmospheric Sciences, Purdue University, USA

<sup>5</sup>NASA/Goddard Institute for Space Studies, USA

<sup>6</sup>Department of Earth and Environmental Science, University of Texas at Arlington, USA

<sup>7</sup>Max Planck Institute for Meteorology, Hamburg, Germany

<sup>8</sup>School of Earth and Environment, University of Leeds, UK

Received: 29 March 2012 – Accepted: 2 April 2012 – Published: 16 April 2012

Correspondence to: D. J. Lunt (d.j.lunt@bristol.ac.uk)

Published by Copernicus Publications on behalf of the European Geosciences Union.

Title Page

Abstract

Introduction

Conclusions

References

Tables

Figures

⏪

⏩

◀

▶

Back

Close

Full Screen / Esc

Printer-friendly Version

Interactive Discussion



## Abstract

The early Eocene (~ 55 to 50 Ma) is a time period which has been explored in a large number of modelling and data studies. Here, using an ensemble of previously published model results, making up “EoMIP” – the Eocene Modelling Intercomparison Project, and syntheses of early Eocene terrestrial and SST temperature data, we present a self-consistent inter-model and model-data comparison. This shows that the previous modelling studies exhibit a very wide inter-model variability, but that at high CO<sub>2</sub>, there is good agreement between models and data for this period, particularly if possible seasonal biases in some of the proxies are considered. An energy balance analysis explores the reasons for the differences between the model results, and suggests that differences in surface albedo feedbacks, water vapour and lapse rate feedbacks, and prescribed aerosol loading are the dominant cause for the different results seen in the models, rather than inconsistencies in other prescribed boundary conditions or differences in cloud feedbacks. The CO<sub>2</sub> level which would give optimal early Eocene model-data agreement, based on those models which have carried out simulations with more than one CO<sub>2</sub> level, is in the range 2000 ppmv to 6500 ppmv. Given the spread of model results, tighter bounds on proxy estimates of atmospheric CO<sub>2</sub> during this time period will allow a quantitative assessment of the skill of the models at simulating warm climates, which could be used as a metric for weighting future climate predictions.

## 1 Introduction

Making robust predictions of future climate change is a major challenge, which has environmental, societal, and economic relevance. The numerical models which are used to make these predictions are normally tested over time periods for which there are extensive instrumental records of climate available, typically over the last ~ 100 yr (Hegerl et al., 2007). However, the variations in climate over these timescales are small relative to the variations predicted for the next 100 yr or more (Meehl et al., 2007), and so

CPD

8, 1229–1273, 2012

EoMIP

D. J. Lunt et al.

Title Page

Abstract

Introduction

Conclusions

References

Tables

Figures

⏪

⏩

◀

▶

Back

Close

Full Screen / Esc

Printer-friendly Version

Interactive Discussion



## EoMIP

D. J. Lunt et al.

Title Page

Abstract

Introduction

Conclusions

References

Tables

Figures

◀

▶

◀

▶

Back

Close

Full Screen / Esc

Printer-friendly Version

Interactive Discussion



likely provide only a weak constraint on future predictions. As such, proxy indicators of climate from older time periods are increasingly being used to test models. On the timescale of  $\sim 100\,000$  yr, the Palaeoclimate Modelling Intercomparison project (PMIP, Braconnot et al., 2007), now in its third phase, is focusing on three main time periods: the mid-Holocene (6000 yr ago, 6 k), the Last Glacial Maximum (LGM, 21 k), and the Last Interglacial (LIG, 125 k). However, these time periods are either colder than modern (LGM), or their warmth is primarily caused not by enhanced greenhouse gases, but by orbital forcing (mid-Holocene, LIG). As such, their use for testing models used for future climate prediction is also limited. On the timescale of millions of years, several time periods show potential for model evaluation, being characterised by substantial warmth which is thought to be driven primarily by enhanced atmospheric  $\text{CO}_2$  concentrations. An example is the mid-Pliocene (3 million years ago, 3 Ma), when global annual temperature was  $\sim 3^\circ\text{C}$  greater than pre-industrial (Dowsett et al., 2009). However the latest estimates of mid-Pliocene  $\text{CO}_2$  (Pagani et al., 2010; Seki et al., 2010) range from  $\sim 360$  to  $\sim 420$  ppmv, which is similar to that of modern ( $\sim 390$  ppmv in 2010 according to the Scripps  $\text{CO}_2$  program, <http://scrippsco2.ucsd.edu/>), and substantially less than typical IPCC scenarios for  $\text{CO}_2$  concentration at the end of this century ( $\sim 1000$  ppmv in the A1F1 scenario,  $> 1370$  ppmv  $\text{CO}_2$ -equivalent in the RCP8.5 scenario, Meehl et al., 2007; Moss et al., 2010). The time period which shows possibly the most similarity to projections of the end of the 21st century and beyond is the early Eocene,  $\sim 55$  to  $\sim 50$  Ma. A recent compilation of Cenozoic atmospheric  $\text{CO}_2$  is relatively data-sparse during the early Eocene, with large uncertainty range, meaning that values more than 2000 ppmv cannot be ruled out (Beerling and Royer, 2011). Relatively high values for the early Eocene are consistent with recent latest Eocene  $\text{CO}_2$  reconstructions of the order 1000 ppmv (Pearson et al., 2009; Pagani et al., 2011). Proxy indicators have been interpreted as showing tropical temperatures at this time  $\sim 5^\circ\text{C}$  warmer than modern (e.g., Pearson et al., 2001), and high latitude terrestrial temperatures more than  $20^\circ\text{C}$  warmer (e.g., Huber and Caballero, 2011). Recently, due at least in part to interest associated with this time period as a possible future

analogue, there have been a number of new sea surface temperature (SST) and terrestrial temperature data published, using a range of proxy reconstruction methods. There have also been several models recently configured for the early Eocene, and attempts made to understand the mechanisms of Eocene warmth. Most of these studies have carried out some form of model-data comparison; however, the models have not been formally intercompared in a consistent framework, and new data now allows a more robust and extensive evaluation of the models.

The aims of this paper are:

- to present an intercomparison of five models, all recently used to simulate the early Eocene climate.
- to carry out a consistent and comprehensive comparison of the model results with the latest proxy temperature indicators, taking full account of uncertainties in the reconstructions.
- by analysing the energy balance and fluxes in the models, to gain an understanding of the reasons behind the differences in the model results.

Section 2 describes the model simulations, Sect. 3 presents the datasets used to evaluate the models, and Sect. 4 presents the model results and model-data comparison. Section 5 quantifies the reasons for the differences between the model results, and Sect. 6 discusses, concludes, and proposes directions for future research.

## 2 Model simulation descriptions

Many model simulations have been carried out over the last two decades with the aim of representing the early Eocene. Here, we present and discuss results from a selection of these. We present all simulations of which we are aware that (a) are published in the peer-reviewed literature, and (b) are carried out with fully dynamic atmosphere-ocean General Circulation Models (GCMs), with primitive-equation atmospheres. This

Title Page

Abstract

Introduction

Conclusions

References

Tables

Figures



Back

Close

Full Screen / Esc

Printer-friendly Version

Interactive Discussion



## EoMIP

D. J. Lunt et al.

Title Page

Abstract

Introduction

Conclusions

References

Tables

Figures

◀

▶

◀

▶

Back

Close

Full Screen / Esc

Printer-friendly Version

Interactive Discussion



makes a total of 4 models – HadCM3L (Lunt et al., 2010), ECHAM5/MPI-OM (Heine-  
mann et al., 2009), CCSM3 (Winguth et al., 2010, 2012; Liu et al., 2009; Huber and  
Caballero, 2011), and GISS ModelE-R (Roberts et al., 2009). Criterion (b) is chosen  
to select the models which are most similar to those used in future climate change  
projection (i.e., we exclude models with energy balance atmospheres such as GENIE  
(Panchuk et al., 2008)). There are two sets of CCSM3 simulations, which we name  
CCSM\_W (Winguth et al., 2010, 2012) and CCSM\_H (Liu et al., 2009; Huber and Ca-  
ballero, 2011). All the models and simulations are summarised in Table 1. Together  
they make up the “Eocene Modelling Intercomparison Project”, EoMIP. EoMIP differs  
from more formal model intercomparisons, such as those carried out under the aus-  
pices of PMIP, in that the groups have carried out their own experimental design and  
simulations in isolation, and the comparison is being carried out post-hoc, rather than  
being planned from the outset. As such, the groups have used different palaeogeog-  
raphical boundary conditions and CO<sub>2</sub> levels to simulate their Eocene climates. This  
has advantages and disadvantages compared to the more formal approach with a sin-  
gle experimental design: the main disadvantage is that a direct comparison between  
models is impossible due to even subtle differences in imposed boundary conditions;  
the main advantage is that in addition to uncertainties in the models themselves, the  
model ensemble also represents the uncertainties in the paleoenvironmental condi-  
tions, and therefore more fully represents the uncertainty in our climatic predictions for  
that time period.

## 2.1 HadCM

Lunt et al. (2010) investigated the potential role of hydrate destabilisation as a mech-  
anism for the Paleocene-Eocene Thermal maximum (PETM, ~ 55Ma), using the  
HadCM3L model. They found a switch in modelled ocean circulation which occurred  
between ×2 and ×4 pre-industrial concentrations of atmospheric CO<sub>2</sub>, which resulted  
in a non-linear warming of intermediate ocean depths. They hypothesised that this  
could be a triggering mechanism for hydrate release. For the 3 Eocene simulations

carried out ( $\times 2$ ,  $\times 4$ , and  $\times 6$ ), vegetation was set globally to a “shrub” plant functional type. The paleogeography is proprietary but is illustrated in Supplementary Information of Lunt et al. (2010). An additional simulation at  $\times 3$   $\text{CO}_2$  was carried out with the same model by Tindall et al. (2010), which incorporated oxygen isotopes into the hydrological cycle. The  $\delta^{18}\text{O}$  of seawater from the Tindall et al. (2010) simulation is used in our SST compilation to inform the uncertainty range of the proxies based on  $\delta^{18}\text{O}$  measurements (see Sect. 3).

## 2.2 ECHAM

Heinemann et al. (2009) presented an ECHAM5/MPI-OM Eocene simulation and compared it to a pre-industrial simulation, diagnosing the reasons for the Eocene warmth by making use of a simple 1-D energy balance model (which we use in this paper in Sect. 5). They reported a larger polar warming than many previous studies, which they attributed to local radiative forcing changes, rather than modified poleward heat transport. The Eocene simulation was carried out under  $\times 2$   $\text{CO}_2$  levels, and a globally homogeneous vegetation was prescribed, with characteristics similar to present-day woody savanna.

## 2.3 CCSM\_W and CCSM\_H

Huber and Caballero (2011) presented a set of Eocene CCSM3 simulations, originally published by Liu et al. (2009), with the main aim of comparing these with a new compilation of proxy terrestrial temperature data. They found that at high  $\text{CO}_2$  ( $\times 16$ ) they obtained good agreement with data from mid and high latitudes. We use this same proxy dataset in this paper, including estimates of uncertainty, for evaluating all the EoMIP simulations.

Winguth et al. (2010) and Winguth et al. (2012) carried out an independent set of CCSM3 simulations motivated by investigating the role of hydrates as a possible cause of the PETM. They found evidence of non-linear ocean warming and enhanced

Title Page

Abstract

Introduction

Conclusions

References

Tables

Figures

⏪

⏩

◀

▶

Back

Close

Full Screen / Esc

Printer-friendly Version

Interactive Discussion



stratification in response to increasing atmospheric CO<sub>2</sub> concentrations, and a shift of deep water formation from northern and southern sources to a predominately southern source.

The CCSM\_W and CCSM\_H simulations differ mainly in the treatment of aerosols. In the CCSM\_W simulation, a high aerosol load is applied, whereas the CCSM\_H simulation considers a lower-than-present-day aerosol distribution following the approach by Kump and Pollard (2008), possibly justified by a reduced ocean productivity and thus reduced DMS emissions. A globally reduced productivity is supported by the recent study of Winguth et al. (2012). However, it remains uncertain to which extent intensified volcanism near the PETM might have increased the aerosol load (Storey et al., 2007).

## 2.4 GISS

Roberts et al. (2009) carried out an investigation into the role of the geometry of Arctic gateways in determining Eocene climate with the GISS ModelE-R. They found that restricting Arctic gateways led to freshening of the Arctic ocean, similar to data associated with the “Azolla” event (Brinkhuis et al., 2006). They incorporated oxygen isotopes into the hydrological cycle in their model, and used the predicted isotopic concentrations of seawater to more directly compare with proxy temperature estimates.

## 3 Early Eocene SST and land temperature datasets

To evaluate the various climate model simulations, we make use of both terrestrial and marine temperature datasets. The marine dataset has been compiled for this paper, the terrestrial data is identical to that presented in Huber and Caballero (2011). In both cases we take as full account as possible of the various uncertainties associated with each proxy.

Title Page

Abstract

Introduction

Conclusions

References

Tables

Figures

⏪

⏩

◀

▶

Back

Close

Full Screen / Esc

Printer-friendly Version

Interactive Discussion



[Title Page](#)[Abstract](#)[Introduction](#)[Conclusions](#)[References](#)[Tables](#)[Figures](#)[⏪](#)[⏩](#)[◀](#)[▶](#)[Back](#)[Close](#)[Full Screen / Esc](#)[Printer-friendly Version](#)[Interactive Discussion](#)

The purpose of these compilations is not to provide a tightly constrained “time-slice” reconstruction of any point in the early Eocene against which the ensemble, or individual model runs can be compared; instead, we include data spanning the entire early Eocene. This approach is consistent with the EoMIP simulations themselves, in which models have not been run with the same specific set of simulation boundary conditions, such as paleogeography or atmospheric greenhouse gas forcings, but can be considered to reflect a possible range of time periods within the early Eocene.

### 3.1 Marine dataset

We have compiled (see Supplementary data) paleotemperature estimates for sea surface (TEX<sub>86</sub>), near-sea surface (mixed layer dwelling planktonic foraminifera) and shallow, inner shelf bottom waters (bivalve oxygen isotopes), from across the early Eocene (Ypresian stage; ~ 55.9 to 49 Ma). This long, ~ 7 Myr time-span includes a significant warming trend in both oceanic intermediate-waters of ~ 4 °C (Zachos et al., 2008), and high-latitude sea surface temperatures of up to ~ 10 °C (Bijl et al., 2009), although tropical sea surface temperatures may have been more stable (Pearson et al., 2007). Also included in the compilation are some data from the very latest Paleocene, within the interval immediately before but not including the Paleocene Eocene Thermal Maximum (PETM). These data are included to increase the geographical coverage of data, especially in the mid to low-latitudes. Given the trend of warming through the early Eocene these pre-PETM data points are likely to represent minimum bounds for estimates of early Eocene temperatures.

For each location with palaeotemperature estimates, the primary geochemical proxy data were collated and then used to generate a set of paleotemperature estimates based on the set of calibrations outlined below. All of the paleotemperature estimation methods used are subject to a range of uncertainty arising from their present-day calibrations, required assumptions about ancient seawater chemistry and potential non-analogue behaviour between the modern and early Paleogene system. Although the latter is very difficult to assess, we make an attempt to quantify uncertainty associated

with the modern calibrations and estimates of ancient seawater chemistry, by determining the upper and lower temperature bounds produced by each proxy method across a reasonable set of calibration equations and parameters (outlined below). To this is added the stated uncertainty determined from the modern calibration data set.

### 3.1.1 Oxygen isotopes

For planktonic foraminifera-derived  $\delta^{18}\text{O}$  temperature estimates we applied the Erez and Luz (1983) calcite  $\delta^{18}\text{O}$  temperature calibration for planktonic foraminifera using both a latitude-corrected estimation of  $\delta^{18}\text{O}_{\text{sw}}$  (Zachos et al., 1994) and a location and depth-specific (mixed-layer;  $\sim 50\text{ m}$  depth in the model) modelled estimation of the oxygen isotopic composition of early Eocene seawater  $\delta^{18}\text{O}_{\text{sw}}$  (Tindall et al., 2010). The published standard error on the Erez and Luz (1983) calibration is  $\pm 1.43^\circ\text{C}$ . For the Eurhomalea and Cucullaea bivalve-derived  $\delta^{18}\text{O}$ , we used the biogenic aragonite  $\delta^{18}\text{O}$ -temperature calibration of Grossman and Ku (1986) as modified by Kobashi et al. (2003), with both the latitude-corrected and modelled  $\delta^{18}\text{O}_{\text{sw}}$  noted above. The published error on the Grossman and Ku (1986) calibration is  $\pm 1.4^\circ\text{C}$ .

### 3.1.2 Mg/Ca ratios of planktonic foraminifera

To estimate calcification temperature, we used the multi-species sediment trap calibration of Anand et al. (2003), which has a calibration standard deviation of  $\pm 1.13^\circ\text{C}$ . This paleotemperature estimation relies strongly upon the assumed value of the Mg/Ca ratio in early Eocene seawater, which is still poorly constrained. There is a considerable disagreement between estimates of Eocene seawater Mg/Ca based on ridge flank hydrothermal carbonate veins, at around  $2\text{ mol mol}^{-1}$  (Coggon et al., 2010) and the 3 to  $4\text{ mol mol}^{-1}$  estimates from paired Mg/Ca and oxygen isotope paleothermometry of deep-sea benthic foraminifera (Lear et al., 2002; and see discussion in Coggon et al., 2011). Within paleoceanographic studies, it has been typical to use values in the range of  $3\text{--}4\text{ mol mol}^{-1}$ , which yield plausible tropical (Sexton et al., 2006) and mid-latitude

[Title Page](#)[Abstract](#)[Introduction](#)[Conclusions](#)[References](#)[Tables](#)[Figures](#)[⏪](#)[⏩](#)[◀](#)[▶](#)[Back](#)[Close](#)[Full Screen / Esc](#)[Printer-friendly Version](#)[Interactive Discussion](#)

(Creech et al., 2010) surface ocean temperatures, consistent with independent paleotemperature estimates. There remains, however, a pressing need to understand the causes of this discrepancy and establish robust estimates of the Mg/Ca ratio of ancient seawater. Here, we calculate paleotemperatures based on two end members of seawater Mg/Ca of 3 and 4 mol mol<sup>-1</sup>. This range is based around the estimate of 3.5 mol mol<sup>-1</sup> calculated by Lear et al. (2002) using their calibration for *Oridorsalis umbonatus* and values of foraminifera Mg/Ca of 2.78 mmol mol<sup>-1</sup> and a  $\delta^{18}\text{O}$ -derived bottom water temperature of 12.4 °C at ~ 49 Ma. The lower, ~ 3 mol mol<sup>-1</sup> value is obtained by the same method, but using revised calibrations for *O. umbonatus* (Rathmann et al., 2004; Rathmann and Kuhnert, 2008). The higher value of 4 mol mol<sup>-1</sup> is in line with older estimates based on attempts to quantify long-term, global trace metal fluxes between the major sources and sinks of Mg and Ca (Wilkinson and Algeo, 1989).

### 3.1.3 TEX<sub>86</sub>

Determining the appropriate calibration of the TEX<sub>86</sub> paleotemperature proxy, based on the relative abundances of several isoprenoid glycerol dibiphytanyl glycerol tetraethers (GDGTs) produced by marine archaeota, to deep-time, warm-climate intervals is an area of active ongoing research. Three methods have recently been proposed based on the same modern calibration data set: separate “low” and “high” temperature proxies based on different ratios of GDGTs, TEX<sub>86</sub><sup>H</sup> and TEX<sub>86</sub><sup>L</sup> (Kim et al., 2010) and a non-linear calibration of the original TEX<sub>86</sub> index (Liu et al., 2009). TEX<sub>86</sub><sup>H</sup> and the Liu et al. (2009) calibrations are based on the same underlying ratio of GDGTs – the original TEX<sub>86</sub> proxy – differing in the form of the calibration equation. Whereas TEX<sub>86</sub><sup>H</sup> and the Liu et al. (2009) calibration maintain a consistent relationship of temperature estimates across the range of TEX<sub>86</sub>, the different ratio of GDGTs within TEX<sub>86</sub><sup>L</sup>, means that it can behave in a fundamentally different manner to these other measures. It is, as yet, unclear which is the most appropriate measure to apply when undertaking deep-time paleotemperature estimation, which may vary across both the temperature (TEX<sub>86</sub>,

[Title Page](#)[Abstract](#)[Introduction](#)[Conclusions](#)[References](#)[Tables](#)[Figures](#)[⏪](#)[⏩](#)[◀](#)[▶](#)[Back](#)[Close](#)[Full Screen / Esc](#)[Printer-friendly Version](#)[Interactive Discussion](#)

TEX<sub>86</sub><sup>L</sup>) range and geographically. New multi-proxy inter-comparisons of these TEX<sub>86</sub> methodologies with oxygen isotope and Mg/Ca paleothermometry suggest that TEX<sub>86</sub><sup>L</sup> produces the best fit to these independent data in mid- to high-latitude locations (Hollis et al., 2012).

For the purposes of this study, we attempt to calculate paleotemperature using all three measures: TEX<sub>86</sub><sup>H</sup>, TEX<sub>86</sub><sup>L</sup> and the Liu et al. (2009) calibration. This provides the full range of temperature estimates produced by all of the most recently proposed TEX<sub>86</sub> proxies and calibrations. In some cases the TEX<sub>86</sub><sup>L</sup> produces clearly erroneous temperature estimates. These can be limited by the exclusion of all analyses with a BIT index in excess of 0.3 (Kim et al., 2010), although they do persist in occasional samples from low-latitude locations (Tanzania). We apply a calibration uncertainty of  $\pm 2.5^{\circ}\text{C}$  to the TEX<sub>86</sub> estimates (Kim et al., 2010). TEX<sub>86</sub> temperature estimates from the Arctic Ocean IODP Site M0004 were undertaken on the early Eocene sequence from Core 27X, which is clearly above the PETM interval, to Core 19X (Sluijs et al., 2008). This sequence is below the termination of the Azolla phase in Core 11X which, from correlations with the North Sea, has been assigned to the basal middle Eocene magnetochron C21r (Sluijs et al., 2008). Data within the hyperthermal interval ETM2 and any data points with BIT indices  $> 0.3$  have also been excluded. Throughout this interval the standard TEX<sub>86</sub> proxies discussed above can be applied to this data rather than the TEX<sub>86</sub><sup>'</sup> proxy used through the PETM (Sluijs et al., 2006).

From this array of time-varying temperature estimates for each site we calculated the median, maximum and minimum values from the time series as the basis for the model-data comparisons. There is an important caveat to this approach that relates to the effect of data quantity and stratigraphic range on the temperature envelopes plotted. Where there is data available across much of the early Eocene, stratigraphic/temporal variability leads to a larger envelope of temperature estimates. Where the data are much more limited in extent, these envelopes are correspondingly smaller. They should thus not be taken to represent “error”, but instead uncertainty associated with temporal variability.

[Title Page](#)[Abstract](#)[Introduction](#)[Conclusions](#)[References](#)[Tables](#)[Figures](#)[◀](#)[▶](#)[◀](#)[▶](#)[Back](#)[Close](#)[Full Screen / Esc](#)[Printer-friendly Version](#)[Interactive Discussion](#)

## 3.2 Terrestrial dataset

For the terrestrial, we make use of the data compilation presented in Huber and Caballero (2011). This is based largely on macrofloral assemblages, with mean annual temperatures being reconstructed primarily by leaf-margin analysis and/or CLAMP. Other proxies are also incorporated, such as isotopic estimates, organic geochemical indicators, and palynoflora. The error bars associated with each data point incorporate uncertainty in calibration, topography, and dating. More information on the data themselves, and the estimates of uncertainty, can be found in Huber and Caballero (2011).

Both marine and terrestrial datasets are provided in Supplementary Information, and are plotted geographically in Figs. 2 and 3, and latitudinally in Figs. 4 and 6. The SST plots show the contributions from the two sources of uncertainty we have considered, related to calibration and temporal trends. This approach to the data aims to include a wide range of potential uncertainties in order to highlight both the regions of potential model-data agreement, but more importantly where there appear to be genuine discrepancies that cannot realistically be explained by the uncertainties in the proxy temperature estimations.

## 4 Results and model-data comparison

In this section, we present results from the EoMIP model ensemble (early Eocene simulations and preindustrial controls), as described in Sect. 2, and compare them with the data described in Sect. 3. The reasons for the different model results are explored in more detail in Sect. 5.

It is useful at this stage to define some nomenclature. To represent the distribution of temperature, we write SST for sea surface temperature (only defined over ocean), or LAT for land near-surface (~ 1.5m) air temperature (only defined over continents), or GAT for near-surface air temperature (defined globally), or GST for surface temperature

CPD

8, 1229–1273, 2012

EoMIP

D. J. Lunt et al.

Title Page

Abstract

Introduction

Conclusions

References

Tables

Figures

⏪

⏩

◀

▶

Back

Close

Full Screen / Esc

Printer-friendly Version

Interactive Discussion



(defined globally), or just  $T$  for a generic temperature. Global means are denoted by angled brackets, so that e.g. the global mean sea surface temperature is  $\langle \text{SST} \rangle$ . Zonal means are denoted by overbars, so that the zonal mean sea surface temperature is  $\overline{\text{SST}}$ . In the case of model output, ensemble means are denoted by square brackets, such as [LAT]. Eocene quantities are given a subscript e, and present/preindustrial (i.e., modern) quantities are given a subscript p. Model values are given a superscript m, and proxy or observed data are given a superscript d. Because the modern observed data has global coverage (albeit interpolated, or assimilated with models in some regions), but the Eocene proxy data is sparse, the modern observed global or zonal means,  $\langle T_p^d \rangle$  and  $\overline{T_p^d}$  are defined, but the Eocene equivalents are not.

#### 4.1 Inter-model comparison

Figure 1 shows the global annual mean sea surface temperature,  $\langle \text{SST} \rangle$ , and global annual mean near-surface land air temperature,  $\langle \text{LAT} \rangle$ , from all the GCM simulations in the EoMIP ensemble, and for modern observations; the Eocene values are also given in Table 2. The observed modern datasets are HadISST for SSTs (pre-industrial; 1850–1890) and NCEP for near-surface air temperatures (present; 1950–1990). For any given  $\text{CO}_2$  level, there is a wide range of modelled Eocene global mean values; for example, at 560 ppmv, there is a  $8.9^\circ\text{C}$  range in  $\langle \text{LAT}_e^m \rangle$  and a  $3.2^\circ\text{C}$  range in  $\langle \text{SST}_e^m \rangle$ . This range is larger than the range of simulated modern global means, which themselves agree well with the observed modern global means. The spread in Eocene results is due to (a) differences in the way the Eocene boundary conditions have been implemented in different models, and (b) different climate sensitivities in the different models. These differences are explored in Sect. 5. The clustering of the pre-industrial results is likely a result of tuning of the pre-industrial simulations to best match observations. For those models with more than one Eocene simulation, the Eocene climate sensitivity ( $\Delta\langle \text{GAT} \rangle$  per  $\text{CO}_2$  doubling) can also be seen to vary, both between models, and also within one model as a function of  $\text{CO}_2$ . The variation of climate sensitivity

between models is well documented in the context of future climate simulations (e.g., IPCC, 2007). The increase in climate sensitivity with CO<sub>2</sub> (for example in the CCSM.H model) is due to the non-linear behavior of climate system feedbacks, for example associated with water vapour (see Sect. 5); however, there is also some non-linearity in the forcing itself as CO<sub>2</sub> increases (Colman and McAveney, 2009). For HadCM, it is also related to a switch in ocean circulation which occurs between ×2 and ×4 CO<sub>2</sub> and is associated with a non-linear increase in surface ocean temperature (Lunt et al., 2010). The HadCM model also carried out an Eocene simulation with ×1 CO<sub>2</sub> (not shown). Comparison of that simulation with its pre-industrial control shows that changing the non-CO<sub>2</sub> boundary conditions to those of the Eocene (i.e., topographic, bathymetric, vegetation, and solar constant changes) results in a 1.8°C increase in global mean surface air temperature, for comparison with a 3.3°C increase for a CO<sub>2</sub> doubling from ×1 to ×2 under Eocene conditions. At a given CO<sub>2</sub> level, the CCSM\_W and CCSM\_H models give quite different global means. This difference in mean Eocene climate state between the two similar models is most mostly due to differences in the assumed Eocene atmospheric aerosol loading; CCSM\_W includes modern aerosols whereas CCSM\_H includes no aerosol loading (see Sect. 2 and Table 1). Both these models share the same pre-industrial simulation. For all models, the ⟨LAT⟩ and ⟨SST⟩ means share similar characteristics, albeit with ⟨SST⟩ varying over a smaller temperature range.

Figure 2 shows the simulated annual mean SST anomaly from each model, and for the proxy reconstructions. A simple anomaly  $SST_e - SST_p$  would not be particularly informative because many regions would be undefined, due to the difference in continental positions between the Eocene and present. Instead, we show  $SST_e - \overline{SST}_p$ , which is only undefined over Eocene continental regions and latitudes at which there is no ocean in the modern. The figures show that some features of temperature change are simulated consistently across models, such as the greatest ocean warming occurring in the mid-latitudes. This mid-latitude maximum is due to reduced SST warming in the high latitudes due to the presence of seasonal seaice anchoring the temperatures

[Title Page](#)[Abstract](#)[Introduction](#)[Conclusions](#)[References](#)[Tables](#)[Figures](#)[⏪](#)[⏩](#)[◀](#)[▶](#)[Back](#)[Close](#)[Full Screen / Esc](#)[Printer-friendly Version](#)[Interactive Discussion](#)

close to 0°C, combined with reduced warming in the tropics due to a lack of snow and seaice albedo feedbacks. However, other patterns are not consistent. For example, GISS at ×4 and HADCM at ×6 have similar values of ⟨SST⟩ relative to their controls (8.6 and 9.0°C, respectively), but the warming in GISS is greatest in the Northeast Pacific and the Southern Ocean, and the warming in HADCM is greatest in the north Atlantic and west of Australia. Similarly, ECHAM at ×2 and CCSM\_H at ×4 have similar global mean SST anomalies (7.2 and 7.8°C, respectively), but the greatest Northern Hemisphere warming is in the Atlantic in ECHAM, but in the Pacific in CCSM\_H. The two CCSM models exhibit similar patterns of warming, correcting for their offset in absolute Eocene temperature – i.e. the patterns of warming in CCSM\_H at ×8 are similar to those in CCSM\_W at ×16 (with anomalies of 10.2 and 10.6°C, respectively).

Figure 3 shows the simulated annual mean LAT anomaly from each model, and for the proxy reconstructions. The anomaly is calculated relative to the pre-industrial (or modern in the case of the proxies) global (land plus ocean) zonal mean air temperature for each model, i.e.  $LAT_e - \overline{GAT}_p$ . The global (as opposed to land-only) zonal mean is used for calculating the anomaly in order to avoid undefined points (for example in the latitudes of the Southern Ocean where there is no land in the modern). Similar to SST, there are some consistent features between models – greatest warming is in the Antarctic (due to the lower topography via the lapse-rate effect and the change in albedo), and there is substantial boreal polar amplification. Again, there are also differences between models. For example, GISS at ×4 and ECHAM at ×2 have similar values of ⟨LAT⟩ relative to their controls (8.5 and 7.3°C, respectively), but GISS has a substantially greater warming over Southeast Asia. These differences cannot be explained solely by differences in topography – the GISS and ECHAM models both use the Eocene topography of Bice and Marotzke (2001).

[Title Page](#)[Abstract](#)[Introduction](#)[Conclusions](#)[References](#)[Tables](#)[Figures](#)[⏪](#)[⏩](#)[◀](#)[▶](#)[Back](#)[Close](#)[Full Screen / Esc](#)[Printer-friendly Version](#)[Interactive Discussion](#)

## 4.2 Model-data comparison

Figure 4 shows a zonal SST model-data comparison for each model. The longitudinal locations of the SST data can be seen in Fig. 2. Each model is capable of simulating Eocene SSTs which are within the uncertainty estimates of the majority of the data points. The data points which lie furthest from the model simulations are the ACEX TEX<sub>86</sub>' Arctic SST estimate (Sluijs et al., 2006), and the  $\delta^{18}\text{O}$  and TEX<sub>86</sub> estimates from New Zealand (Bijl et al., 2009). The Arctic temperature reconstructions have uncertainty estimates which mean that at high CO<sub>2</sub> ( $\times 8\text{--}16$ ), the CCSM\_H and CCSM\_W model simulations are just within agreement. At this CO<sub>2</sub> level, these models are also consistent with the tropical temperature estimates. From Fig. 1a, it is likely that other models could also obtain similarly high Arctic temperatures, if they were run at sufficiently high CO<sub>2</sub> or low aerosol forcing. Also, given that some of these models (e.g., HadCM) have a higher climate sensitivity than CCSM\_H, this model-data consistency could be potentially obtained at a lower CO<sub>2</sub> than in CCSM\_H.

TEX<sub>86</sub> is a relatively new proxy, which, as discussed in Sect. 3, is currently undergoing a process of rapid development. In this context, it has been suggested that the proxy could be recording the palaeotemperature anomaly of the bloom season of the marine archaeota, as opposed to a true annual mean. If this is the case, then it is likely that a more appropriate comparison is with the modelled summer temperature. This is illustrated in Fig. 5, for the HadCM model. In this case, the modelled warm month mean temperature for the highest CO<sub>2</sub> ( $\times 6$ ) is within the uncertainty range of the Arctic TEX<sub>86</sub> temperatures.

Figure 6 shows the terrestrial temperature model-data comparison for each model. Those models which have been run at high CO<sub>2</sub> (both CCSM models), show good agreement with the data across all latitudes. The other models do not simulate such high temperatures, but, as with SST, it does appear that if they had been run at higher CO<sub>2</sub>, the model-data agreement would have been better. The HadCM model appears to be somewhat of an outlier in the Northern Hemisphere high latitudes, as it shows

[Title Page](#)[Abstract](#)[Introduction](#)[Conclusions](#)[References](#)[Tables](#)[Figures](#)[◀](#)[▶](#)[◀](#)[▶](#)[Back](#)[Close](#)[Full Screen / Esc](#)[Printer-friendly Version](#)[Interactive Discussion](#)

less polar amplification than the other models (see Sect. 4.3), an effect also seen in SST.

A quantitative indication of the model-data comparison for each simulation cannot currently be used to rank the models themselves, because the actual CO<sub>2</sub> forcing is not well constrained by data. However, it could give an indication of the range of CO<sub>2</sub> concentrations which are most consistent with the data. Given the sparseness of the SST and terrestrial data, any score should be treated with some caution. This is compounded by the uneven spread of the data; for example, there is a relatively high concentration of terrestrial data in North America. There are also issues associated with the different land-sea masks in the different models, which mean that the number of proxy data locations at which there are defined modelled values differs between the models. Therefore, we generate a simple mean-error score for each simulation,  $\sigma$ , for both SST ( $\sigma_{\text{sst}}$ ) and land air temperature ( $\sigma_{\text{lat}}$ ), by averaging the error in temperature anomaly at the location of each of  $N$  data points:

$$\sigma_{\text{sst}} = \frac{1}{N} \sum \left( \text{SST}_e^m - \overline{\text{SST}_p^m} - \text{SST}_e^d + \overline{\text{SST}_p^d} \right), \quad (1)$$

$$\sigma_{\text{lat}} = \frac{1}{N} \sum \left( \text{LAT}_e^m - \overline{\text{GAT}_p^m} - \text{LAT}_e^d + \overline{\text{GAT}_p^d} \right), \quad (2)$$

but proceed with caution, being mindful that there is a considerable uncertainty in the score itself. Values of  $\sigma$  for each model simulation are given in Table 2. For each model, the best results are obtained for the highest CO<sub>2</sub> level which was simulated (a result which also applies if an RMS score is used in place of a mean error score). The CCSM\_H model at 16× CO<sub>2</sub> has the best (i.e., lowest absolute) values of  $\sigma$ . However, as noted before, it appears that other models would also obtain good  $\sigma$  scores if they had been run at sufficiently high CO<sub>2</sub>. A “best-case” multi-model ensemble can be created by averaging the simulations from each model which have the lowest values of  $\sigma$  (it turns out that those models with the best  $\sigma_{\text{lat}}$  also have the best  $\sigma_{\text{sst}}$ ). These are the models highlighted in bold in Table 2. The model-data comparison for this multi-model

ensemble is shown in Figs. 7 and 8. The 2 standard-deviation width of the “best-case” ensemble overlaps the uncertainty estimates of every terrestrial and ocean proxy data point. However, the high latitude New Zealand SST estimates are right at the boundary of consistency. The terrestrial data shows very good agreement with the model ensemble, and both data and models show a similar degree of polar amplification (see Sect. 4.3).

By regressing the CO<sub>2</sub> levels and  $\sigma$  values in Table 2, it is possible (for those models with more than one Eocene simulation) to provide a first-order estimate of the CO<sub>2</sub> level, for each model, which could give the best agreement with the proxy estimates. For HadCM, CCSM\_H, and CCSM\_W, using  $\sigma_{sst}$  this is 2100 ppmv, 4100 ppmv, and 5400 ppmv, respectively, and using  $\sigma_{lat}$  this is 2800 ppmv, 4500 ppmv, and 6300 ppmv, respectively. These estimates come with many caveats, not least that the uneven and sparse data spread means that the absolute minimum mean error,  $\sigma$ , is not necessarily a good indicator of the correct global mean temperature. However, they do indicate the magnitude of the range of CO<sub>2</sub> values that could be considered consistent with model results. These values are significantly higher than those presented for this time period in the compilation of Beerling and Royer (2011).

### 4.3 Meridional gradients and polar amplification

The changes in meridional temperature gradient are summarised in Fig. 9, which shows the surface temperature difference between the low latitudes ( $|\phi| < 30^\circ$ ) and the high latitudes ( $|\phi| > 60^\circ$ ) as a function of global mean temperature, and how this is partitioned between land and ocean warming (Fig. 9b). All the Eocene simulations have a reduced meridional surface temperature gradient compared with the pre-industrial, and the gradient reduces further as CO<sub>2</sub> increases, i.e. polar amplification increases (Fig. 9a). However, there is a high degree of inter-model variability in the absolute Eocene gradient, with HadCM appearing to be an outlier with a relatively high Eocene gradient. There is some indication that the models are asymptoting towards a minimum gradient of about 20°C. This, along with our energy flux analysis (see Sect. 5),

Title Page

Abstract

Introduction

Conclusions

References

Tables

Figures

⏪

⏩

◀

▶

Back

Close

Full Screen / Esc

Printer-friendly Version

Interactive Discussion



[Title Page](#)[Abstract](#)[Introduction](#)[Conclusions](#)[References](#)[Tables](#)[Figures](#)[◀](#)[▶](#)[◀](#)[▶](#)[Back](#)[Close](#)[Full Screen / Esc](#)[Printer-friendly Version](#)[Interactive Discussion](#)

supports previous work (Huber et al., 2003) that implied that meridional temperature gradients of the order  $20^{\circ}\text{C}$  were physically realistic, even without large changes to meridional heat transport. Compared with preindustrial, the meridional surface temperature gradient reduces more on land than over ocean (Fig. 9b). For HadCM, this applies also to the Eocene simulations as  $\text{CO}_2$  increases. However, for the two CCSM models, the meridional temperature gradient is reduced by a similar amount over land and ocean as a function of  $\text{CO}_2$ , with some indication, at maximum ( $\times 16$ )  $\text{CO}_2$ , that the SST gradient starts reducing more over ocean than over land. This implies that when considering changes relative to the modern, it is possible to have substantially different temperature changes over land compared with over ocean at the same latitude. This is also clear from comparing Fig. 2 with Fig. 3, and shows the importance of differentiating terrestrial and oceanic signals when considering the consistency between different proxy data, and between data and models.

## 5 Reasons for inter-model variability: an energy flux analysis

It is interesting up to a point to simply intercompare model results, and to compare with data, but also of interest is to know *why* different models behave differently. Given the complexity of climate models, this can be problematic, and traditionally, groups such as PMIP have not often diagnosed in detail the differences. Here, we attempt to diagnose some aspects of the differences between the model results, building on a 1-D energy-balance approach as outlined by Heinemann et al. (2009). Here, the causes of the zonal-mean temperature response of a model are diagnosed from the top-of-the-atmosphere and surface radiative fluxes, including their clear-sky values, assuming simple energy balance. Any difference between the meridional temperature profile in the GCM, and that estimated from the energy-balance approach, is attributed to meridional heat transport. As such, the change in meridional temperature profile between two simulations (such as a pre-industrial control and an Eocene simulation) can be attributed to a combination of (1) changes in emissivity due to changes in clouds,

(2) changes in emissivity due to changes in the greenhouse effect (i.e., CO<sub>2</sub> and water vapour concentration changes, and lapse-rate effects), (3) changes in albedo due to changes in clouds, (4) changes in albedo due to Earth-surface and atmospheric aerosol changes, and (5) changes in meridional heat transport.

5 Following Heinemann et al. (2009), the 1-D energy balance model (EBM) is formulated by equating the incoming solar radiation with outgoing long wave radiation, with any local imbalance attributed to local meridional heat transport:

$$SW_t^\downarrow(1 - \alpha) - H = \epsilon\sigma\tau^4 \quad (3)$$

10 where  $SW_t^\downarrow$  is the incoming solar radiation at the top of the atmosphere,  $\alpha$  is the planetary albedo,  $H$  is the net meridional heat transport divergence,  $\epsilon$  is the atmospheric emissivity,  $\sigma$  is the Stephan-Boltzmann constant, and  $\tau$  is the surface temperature, to be diagnosed by the EBM. All variables are functions of latitude apart from  $\sigma$ . The planetary albedo is given by

$$\alpha = \frac{SW_t^\uparrow}{SW_t^\downarrow} \quad (4)$$

15 and the atmospheric emissivity is given by

$$\epsilon = \frac{LW_t^\uparrow}{LW_s^\uparrow}, \quad (5)$$

20 where  $SW_t^\uparrow$  and  $SW_t^\downarrow$  are the outgoing and incoming top of the atmosphere shortwave radiation, respectively, and  $LW_t^\uparrow$  and  $LW_s^\uparrow$  are the upwelling top of the atmosphere and surface longwave radiation, respectively. Given that the surface emits long wave radiation according to

$$LW_s^\uparrow = \sigma\tau^4, \quad (6)$$

Title Page

Abstract

Introduction

Conclusions

References

Tables

Figures

⏪

⏩

◀

▶

Back

Close

Full Screen / Esc

Printer-friendly Version

Interactive Discussion



it follows that the meridional heat transport divergence,  $H$ , is given by

$$H = +(\text{SW}_t^{\text{net}} + \text{LW}_t^{\text{net}}), \quad (7)$$

where the superscript net represents net flux (positive downwards). N.B. the “+” sign in this equation, which was wrongly given as “-” in the equivalent equation in Heinemann et al. (2009). All the radiative fluxes are output directly from the GCMs, and used as input into the energy balance model. From Eq. (3), it follows that

$$\tau = \left( \frac{1}{\epsilon\sigma} (\text{SW}_t^{\downarrow} (1 - \alpha) - H)^{0.25} \right) \equiv E(\epsilon, \alpha, H). \quad (8)$$

The difference in temperature between two simulations,  $\Delta T = \tau - \tau'$  is given by  $E(\epsilon, \alpha, H) - E(\epsilon', \alpha', H')$ , where the prime, ' , represents values in the second simulation. In order to diagnose the reasons for the temperature differences in two simulations, we consider changes to the diagnosed emissivity, planetary albedo, and heat transport, and write,

$$\Delta T_{\text{emm}} = E(\epsilon, \alpha, H) - E(\epsilon', \alpha, H) \quad (9)$$

$$\Delta T_{\text{alb}} = E(\epsilon, \alpha, H) - E(\epsilon, \alpha', H) \quad (10)$$

$$\Delta T_{\text{tran}} = E(\epsilon, \alpha, H) - E(\epsilon, \alpha, H'), \quad (11)$$

where  $\Delta T_{\text{emm}}$ ,  $\Delta T_{\text{alb}}$ , and  $\Delta T_{\text{tran}}$  are the components of  $\Delta T$  due to emissivity, planetary albedo, and heat transport changes, respectively. Because the changes in emissivity, albedo, and heat transport are relatively small compared to their magnitude,

$$\Delta T \simeq \Delta T_{\text{emm}} + \Delta T_{\text{alb}} + \Delta T_{\text{tran}}. \quad (12)$$

We further partition the  $\Delta T_{\text{emm}}$  and  $\Delta T_{\text{alb}}$  terms by considering the clear-sky radiative fluxes, also output directly from the GCMs. Using cs as a subscript to denote clear-sky fluxes, we can estimate the contribution due to the greenhouse effect ( $\text{CO}_2$  and water

Title Page

Abstract

Introduction

Conclusions

References

Tables

Figures

◀

▶

◀

▶

Back

Close

Full Screen / Esc

Printer-friendly Version

Interactive Discussion



vapour and lapse rate) changes,  $\Delta T_{\text{gg}}$ , and the contribution due to surface albedo and aerosol changes,  $\Delta T_{\text{salb}}$ ,

$$\Delta T_{\text{gg}} = E(\epsilon_{\text{CS}}, \alpha_{\text{CS}}, H_{\text{CS}}) - E(\epsilon'_{\text{CS}}, \alpha_{\text{CS}}, H_{\text{CS}}) \quad (13)$$

$$\Delta T_{\text{salb}} = E(\epsilon_{\text{CS}}, \alpha_{\text{CS}}, H_{\text{CS}}) - E(\epsilon_{\text{CS}}, \alpha'_{\text{CS}}, H_{\text{CS}}) \quad (14)$$

because the emissivity change in the clear-sky case is solely due to greenhouse effect changes, and the albedo change in the clear-sky case is mainly due to surface albedo and aerosols. Considering the remaining temperature difference as due to clouds, we can then write

$$\Delta T_{\text{lwc}} = \Delta T_{\text{emm}} - \Delta T_{\text{gg}} \quad (15)$$

$$\Delta T_{\text{swc}} = \Delta T_{\text{alb}} - \Delta T_{\text{salb}}, \quad (16)$$

where  $\Delta T_{\text{lwc}}$  and  $\Delta T_{\text{swc}}$  are the components of  $\Delta T$  due to long-wave cloud changes and short-wave cloud changes, respectively. In this way, a temperature difference between two simulations can be partitioned into 5 components, given by Eqs. (9)–(11) and (13)–(16).

Figure 10 shows the results from this energy balance analysis, for a number of pairs of simulations. Figure 10a–c shows the models which simulate a transition from pre-industrial to Eocene at  $\times 2 \text{ CO}_2$ . ECHAM and CCSM\_H show similar results in terms of the reasons for this change. They show a high latitude warming in both hemispheres caused mainly by non-cloud albedo changes, with a significant contribution also from emissivity changes. In both these models, short-wave cloud albedo changes act to reduce the polar amplification in both hemispheres. The greater global temperature change in ECHAM compared with CCSM\_H is due to the greater change in greenhouse effect. However, the energy balance analysis does not allow us to diagnose if this is due to a greater radiative forcing given the same  $\text{CO}_2$  increase, or due to greater water vapour feedbacks or lapse-rate changes in ECHAM. HadCM exhibits quite different behavior. In the Southern Hemisphere, the zonal mean temperature increase is

Title Page

Abstract

Introduction

Conclusions

References

Tables

Figures

⏪

⏩

◀

▶

Back

Close

Full Screen / Esc

Printer-friendly Version

Interactive Discussion



## EoMIP

D. J. Lunt et al.

[Title Page](#)[Abstract](#)[Introduction](#)[Conclusions](#)[References](#)[Tables](#)[Figures](#)[Back](#)[Close](#)[Full Screen / Esc](#)[Printer-friendly Version](#)[Interactive Discussion](#)

due predominantly to non-cloud albedo changes, and is reduced relative to the other two models. In the Northern Hemisphere, the increase in temperature is much reduced relative to the other two models, due to a lack of non-cloud albedo feedbacks, and changes in emissivity. Abbot and Tziperman (2008) suggested that the lack of sea ice in the Arctic can lead to stronger convection over the relatively warm Arctic sea surface during winter, leading to more convective clouds and increased water vapour concentrations, and thereby causing polar amplification via both albedo and emissivity effects. The largely decreased (versus unchanged) surface albedo in northern high latitudes in CCSM\_H and ECHAM (versus HadCM), increased (versus virtually unchanged) long-wave cloud radiative forcing, and reduced (versus hardly changed) clear-sky emissivity indicates that this seaice/convection feedback is active for  $\times 1$  to  $\times 2$  in CCSM\_H and ECHAM, but absent in HadCM.

Figure 10d–g shows the models which simulate a transition from pre-industrial to Eocene at  $\times 4$  CO<sub>2</sub>. For HadCM and CCSM\_H, the results are very similar to at  $\times 2$  CO<sub>2</sub>, but with greater magnitude; for both models each component contributes the same fraction to the total warming under  $\times 2$  as to under  $\times 4$ , to within 10%. CCSM\_W is very similar to CCSM\_H, except that it has reduced warming due to decreased change in non-cloud albedo. This is most likely a direct result of the different aerosol fields applied in the these two models for the Eocene (see Table 1). The model which exhibits the greatest warming is the GISS model. This high sensitivity relative to the other models is due to greater greenhouse gas forcing, and greater cloud albedo feedbacks. The warming over Antarctica is particularly large in the GISS model, and is due to a greater local change in non-cloud albedo. However, the GISS model also has strong negative cloud forcing at high latitudes in both hemispheres.

Figure 10h,i shows the models which simulate a transition from  $\times 2$  to  $\times 4$  CO<sub>2</sub> under Eocene conditions. HadCM has a greater climate sensitivity than CCSM\_H, and this is due to greater changes in greenhouse gas emissivity, and a positive as opposed to negative cloud albedo feedback. The relative lack of polar amplification in both models compared to the results discussed above, is due to the lack of Antarctic ice sheet in the

Eocene. The small amount of polar amplification in HadCM is due to changes in heat transport; in CCSM it is due to non-cloud albedo changes in the Northern Hemisphere.

Figure 10j,k shows the models which simulate a transition from  $\times 4$  to  $\times 8$   $\text{CO}_2$  under Eocene conditions. Similar to the transition from  $\times 2$  to  $\times 4$ , the polar amplification is relatively small. The warming is due almost entirely to the changes in emissivity (direct  $\text{CO}_2$  forcing and water vapour feedbacks and lapse-rate changes), and unsurprisingly has a similar latitudinal distribution in the two models. However, in the Northern Hemisphere high latitudes the CCSM\_H model shows strong opposing effects of cloud and surface changes, which are not present in CCSM\_W. This is most likely due to the remnants of Arctic sea ice in CCSM\_W at  $\times 8$   $\text{CO}_2$  which are not present in the warmer CCSM\_H model. Comparison of Fig. 10k with Fig. 10i shows that the increase in climate sensitivity in CCSM\_H as a function of background  $\text{CO}_2$  is due almost entirely to increased non-cloud emissivity changes; the framework does not allow us to determine if this is due to increasing radiative effects due to  $\text{CO}_2$ , or increasing water vapour feedbacks or lapse-rate changes. However, it is clear that it is not due to increased albedo feedbacks, or cloud processes.

Given that the models prescribe Eocene vegetation in quite different ways, it is interesting to assess how much this affects inter-model variability. Figure 11 shows the surface albedo in the pre-industrial control and the  $\times 2$   $\text{CO}_2$  simulations for HadCM, CCSM\_H, and ECHAM. At the high latitudes, this is affected by snow and sea ice cover and prescribed changes in ice sheets, but at low latitudes this is purely a result of the imposed vegetation and open-ocean albedos. The fact that all the models have a low latitude albedo which is similar to their control, and similar to each other, indicates that this aspect of experimental design is likely not playing an important role in determining the differences in results between the models.

[Title Page](#)[Abstract](#)[Introduction](#)[Conclusions](#)[References](#)[Tables](#)[Figures](#)[⏪](#)[⏩](#)[◀](#)[▶](#)[Back](#)[Close](#)[Full Screen / Esc](#)[Printer-friendly Version](#)[Interactive Discussion](#)

## 6 Conclusions and outlook

We have carried out an intercomparison and model-data comparison of the results from 5 early Eocene modelling studies, using 4 different climate models. The model results show a large spread in global mean temperatures, for example a  $\sim 9^\circ\text{C}$  range in surface air temperature under a single  $\text{CO}_2$  value, and are characterised by warming in different regions. The models which have been run at sufficiently high  $\text{CO}_2$  show very good agreement with the terrestrial data. The comparison with SST data is also good, but the model and data uncertainty only just overlap for the Arctic and New Zealand  $\delta^{18}\text{O}$  and  $\text{TEX}_{86}$  proxies. However, if a possible seasonality bias in the proxies is taken into account, then the model data agreement improves further. We have interrogated the reasons for the differences between the models, and found differences in climate sensitivity to be due primarily to a combination of greenhouse effect and surface albedo feedbacks, rather than differences in heat transport or cloud feedbacks.

There are several issues which have emerged from this study, which should be addressed in future work aimed at reconciling model simulations and proxy data reconstructions of the Early Eocene (many of which also apply to other time periods).

Firstly, modelling groups should aim to carry out simulations over a wider range of atmospheric  $\text{CO}_2$  levels. In particular, the results of CCSM\_H indicate that at high prescribed atmospheric  $\text{CO}_2$  and low aerosol forcing, the models and data come close together. Some of this work is in progress (e.g. simulations at  $\times 3 \text{ CO}_2$  are currently being analysed for the ECHAM model). However, it should be noted that this is not always possible. For example, the Eocene HadCM model has been run at  $\times 8 \text{ CO}_2$ , but after about 2700 yr the model developed a runaway greenhouse, and the model eventually crashed (Lunt et al., 2007). A similar effect has been observed in the ECHAM model at  $\times 4 \text{ CO}_2$  (Heinemann, 2009). Whether such an effect is “real”, i.e. whether the real world would also develop a runaway greenhouse, is completely unknown. In any case, it is clear that modelling the early Eocene climate pushes the climate model

CPD

8, 1229–1273, 2012

EoMIP

D. J. Lunt et al.

Title Page

Abstract

Introduction

Conclusions

References

Tables

Figures

◀

▶

◀

▶

Back

Close

Full Screen / Esc

Printer-friendly Version

Interactive Discussion



parameterisations to the boundaries within which they were designed to operate, if not beyond these boundaries.

Some of the differences between the model results can be attributed to differences in the experimental design. In particular, some models apply a very generic Eocene vegetation, which is not particularly realistic. A slightly more coordinated study could provide guidelines for ways to better represent Eocene vegetation, for example by making use of palynological data, or by using dynamic vegetation models where available. This would provide an ensemble of model results which better represented the true uncertainty in our model simulations. Other inconsistencies between model simulations should not necessarily be eliminated – for example, different models using different paleogeographical reconstructions may be more representative of the true spread of model results than if all groups used a single paleogeography.

On the data side, better understanding of the temperature proxies and their associated uncertainties, in particular seasonal effects, is a clear goal for future work, as is greater geographical and finer temporal coverage.

Perhaps most crucial of all, better CO<sub>2</sub> constraints from proxies would be of huge benefit to model-data comparison exercises such as this. Recently, much work is being undertaken in this area, but this should be intensified wherever possible. We note that at high CO<sub>2</sub>, due to the logarithmic nature of the CO<sub>2</sub> forcing, proxies which may have relatively coarse precision at low CO<sub>2</sub>, can actually provide very strong constraints on the CO<sub>2</sub> forcing itself. Such constraints on CO<sub>2</sub>, combined with proxy temperature reconstructions with well defined uncertainty ranges, could provide a strong constraint on model simulations, providing quantitative metrics for assessing model performance, and could ultimately provide relative weightings for model simulations of future climates.

**Supplementary material related to this article is available online at:**  
<http://www.clim-past-discuss.net/8/1229/2012/cpd-8-1229-2012-supplement.zip>.



*Acknowledgements.* This paper resulted from discussions at the “CO<sub>2</sub> at the zoo” event held in Bristol in 2010, and from a Royal Society Kavli meeting held in 2011. DJL acknowledges funding as an RCUK research fellow.

## References

- 5 Abbot, D. S. and Tziperman, E.: Sea Ice, High Latitude Convection, and Equable Climates, *Geophys. Res. Lett.*, 35, L03702, doi:10.1029/2007GL032286, 2008.
- Anand, P., Elderfield, H., and Conte, M.: Calibration of Mg/Ca thermometry in planktonic foraminifera from a sediment trap time series, *Paleoceanography*, 18, 1050, doi:10.1029/2002PA000846, 2003. 1237
- 10 Beerling, D. and Royer, D.: Convergent Cenozoic CO<sub>2</sub> history, *Nat. Geosci.*, 4, 418–420, 2011. 1231, 1246
- Bice, K. L. and Marotzke, J.: Numerical evidence against reversed thermohaline circulation in the warm Paleocene/Eocene ocean, *J. Geophys. Res.*, 106, 11529–11542, 2001. 1243, 1261
- 15 Bijl, P. K., Schouten, S., Sluijs, A., Reichert, G.-J., Zachos, J. C., and Brinkhuis, H.: Early Palaeogene temperature evolution of the southwest Pacific Ocean, *Nature*, 461, 776–779, 2009. 1236, 1244
- Braconnot, P., Otto-Bliesner, B., Harrison, S., Joussaume, S., Peterchmitt, J.-Y., Abe-Ouchi, A., Crucifix, M., Driesschaert, E., Fichet, Th., Hewitt, C. D., Kageyama, M., Kitoh, A., Laine, A., Loutre, M.-F., Marti, O., Merkel, U., Ramstein, G., Valdes, P., Weber, S. L., Yu, Y., and Zhao, Y.: Results of PMIP2 coupled simulations of the Mid-Holocene and Last Glacial Maximum – Part 1: experiments and large-scale features, *Clim. Past*, 3, 261–277, doi:10.5194/cp-3-261-2007, 2007. 1231
- 20 Coggon, R. M., Teagle, D. A. H., Smith-Duque, C. E., Alt, J. C., and Cooper, M. J.: Reconstructing past seawater Mg/Ca and Sr/Ca from mid-ocean ridge flank calcium carbonate veins, *Science*, 327, 1114–1117, 2010. 1237
- 25 Coggon, R. M., Teagle, D. A. H., and Jones, T. D.: Comment on What do we know about the evolution of Mg to Ca ratios in seawater? by Wally Broecker and Jimin Yu, *Paleoceanography*, 26, PA3224, doi:10.1029/2011PA002186, 2011. 1237

Title Page

Abstract

Introduction

Conclusions

References

Tables

Figures

◀

▶

◀

▶

Back

Close

Full Screen / Esc

Printer-friendly Version

Interactive Discussion



[Title Page](#)[Abstract](#)[Introduction](#)[Conclusions](#)[References](#)[Tables](#)[Figures](#)[◀](#)[▶](#)[◀](#)[▶](#)[Back](#)[Close](#)[Full Screen / Esc](#)[Printer-friendly Version](#)[Interactive Discussion](#)

- Collins, W. D., Bitz, C. M., Blackmon, M. L., Bonan, G. B., Bretherton, C. S., Carton, J. A., Chang, P., Doney, S. C., Hack, J. J., Henderson, T. B., Kiehl, J. T., Large, W. G., Mckenna, D. S., Santer, B. D., and Smith, R. D.: The Community Climate System Model Version 3 (CCSM3), *J. Climate*, 19, 2122–2143, 2006. 1261
- 5 Colman, R. and McAveney, B.: Climate feedbacks under a very broad range of forcing, *Geophys. Res. Lett.*, 36, L01702, doi:10.1029/2008GL036268, 2009. 1242
- Cox, P. M., Betts, R. A., Jones, C. D., Spall, S. A., and Totterdell, I. J.: Modelling vegetation and the carbon cycle as interactive elements of the climate system, in: *Meteorology at the Millennium*, edited by: Pearce, R., Academic Press, 259–279, 2001. 1261
- 10 Creech, J. B., Baker, J. A., Hollis, C. J., Morgans, H. E. G., and Smith, E. G. C.: Eocene sea temperatures for the mid-latitude Southwest Pacific from Mg/Ca ratios in planktonic and benthic foraminifera, *Earth Planet. Sci. Lett.*, 299, 483–495, 2010. 1238
- Dowsett, H. J., Robinson, M. M., and Foley, K. M.: Pliocene three-dimensional global ocean temperature reconstruction, *Clim. Past*, 5, 769–783, doi:10.5194/cp-5-769-2009, 2009. 1231
- 15 Erez, J. and Luz, B.: Experimental paleotemperature equation for planktonic foraminifera, *Geochim. Cosmochim. Ac.*, 47, 1025–1031, 1983. 1237
- Grossman, E. and Ku, T. L.: Oxygen and carbon isotope fractionation in biogenic aragonite: temperature effects, *Chem. Geol.*, 59, 59–74, 1986. 1237
- Hegerl, G. C., Zwiers, F. W., Braconnot, P., Gillett, N. P., Luo, Y., Orsini, J. A. M., Nicholls, N., Penner, J. E., and Stott, P. A.: Understanding and attributing climate change, in: *Climate Change 2007: The Physical Science Basis. Contribution of Working Group I to the Fourth Assessment Report of the Intergovernmental Panel on Climate Change*, Cambridge University Press, 2007. 1230
- 20 Heinemann, M.: Warm and sensitive Paleocene-Eocene climate, *Reports on Earth System Science*, Max Planck Institute for Meteorology, Hamburg, 70, 2009. 1253
- Heinemann, M., Jungclaus, J. H., and Marotzke, J.: Warm Paleocene/Eocene climate as simulated in ECHAM5/MPI-OM, *Clim. Past*, 5, 785–802, doi:10.5194/cp-5-785-2009, 2009. 1233, 1234, 1247, 1248, 1249, 1261
- Huber, M. and Caballero, R.: The early Eocene equable climate problem revisited, *Clim. Past*, 7, 603–633, doi:10.5194/cp-7-603-2011, 2011. 1231, 1233, 1234, 1235, 1240, 1261, 1268
- 30 Kim, J.-H., Meer, J. V. D., Schouten, S., Helmke, P., Willmott, V., Sangiorgi, F., Koç, N., Hopmans, E. C., and Damsté, J. S. S.: New indices and calibrations derived from the distribution

## EoMIP

D. J. Lunt et al.

Title Page

Abstract

Introduction

Conclusions

References

Tables

Figures

◀

▶

◀

▶

Back

Close

Full Screen / Esc

Printer-friendly Version

Interactive Discussion



of crenarchaeal isoprenoid tetraether lipids: Implications for past sea surface temperature reconstructions, *Geochim. Cosmochim. Ac.*, 74, 4639–4654, 2010. 1238, 1239

Kobashi, T., Grossman, E., Yancey, T. E., and Dockery, D. T.: The oxygen isotopic record of seasonality in *Conus* shells and its applications to understanding the late middle Eocene (38 Ma) climate, *Paleontol. Res.*, 7, 343–355, 2003. 1237

Kump, L. R. and Pollard, D.: Amplification of cretaceous warmth by biological cloud feedbacks, *Science*, 320, 195, 2008. 1235

Lear, C., Rosenthal, Y., and Slowey, N.: Benthic foraminiferal Mg/Ca-paleothermometry: a revised core-top calibration, *Geochim. Cosmochim. Ac.*, 66, 3375–3387, 2002. 1237, 1238

Liu, Z., Pagani, M., Zinniker, D., DeConto, R. M., Huber, M., Brinkhuis, H., Shah, S. R., Leckie, R. M., and Pearson, A.: Global cooling during the Eocene-Oligocene climate transition, *Science*, 323, 1187–1190, 2009. 1233, 1234, 1238, 1239, 1261

Lunt, D. J., Valdes, P. J., and Ridgwell, A.: On the linearity of climate sensitivity: a case study for the future and the PETM, AGU poster, available at: [http://www.paleo.bris.ac.uk/~ggdj/conferences/agu2007\\_climsens.pdf](http://www.paleo.bris.ac.uk/~ggdj/conferences/agu2007_climsens.pdf), 2007. 1253

Lunt, D. J., Valdes, P. J., Dunkley-Jones, T., Ridgwell, A., Haywood, A. M., Schmidt, D. N., Marsh, R., and Maslin, M.: CO<sub>2</sub>-driven ocean circulation changes as an amplifier of Paleocene-Eocene thermal maximum hydrate destabilization, *Geology*, 38, 875–878, 2010. 1233, 1234, 1242, 1261

Meehl, G. A., Stocker, T. F., Collins, W. D., Friedlingstein, W. D. C., Gaye, A. T., Gregory, J. M., Kitoh, A., Knutti, R., Murphy, J. M., Noda, A., Raper, S. C. B., Watterson, I. G., Weaver, A. J., and Zhao, Z.-C.: Global climate projections, in: *Climate Change 2007: The Physical Science Basis. Contribution of Working Group I to the Fourth Assessment Report of the Intergovernmental Panel on Climate Change*, Cambridge University Press, 2007. 1230, 1231

Moss, R. H., Edmonds, J. A., Hibbard, K. A., Manning, M. R., Rose, S. K., van Vuuren, D. P., Carter, T. R., Emori, S., Kainuma, M., Kram, T., Meehl, G. A., Mitchell, J. F. B., Nakicenovic, N., Riahi, K., Smith, S. J., Stouffer, R. J., Thomson, A. M., Weyant, J. P., and Wilbanks, T. J.: The next generation of scenarios for climate change research and assessment, *Nature*, 463, 747–756, 2010. 1231

Pagani, M., Liu, Z., LaRiviere, L., and Ravelo, A. C.: High Earth-system climate sensitivity determined from Pliocene carbon dioxide concentrations, *Nat. Geosci.*, 3, 27–30, 2010. 1231

- Pagani, M., Huber, M., Liu, Z., Bohaty, S. M., Henderiks, J., Sijp, W., Krishnan, S., and De-Conto, R. M.: The role of carbon dioxide during the onset of Antarctic glaciation, *Science*, 334, 1261–1264, 2011. 1231
- Panchuk, K., Ridgwell, A., and Kump, L. R.: Sedimentary response to Paleocene-Eocene thermal maximum carbon release: a model-data comparison, *Geology*, 36, 315–318, 2008. 1233
- Pearson, P. N., Ditchfield, P. W., Singano, J., Harcourt-Brown, K. G., Nicholas, C. J., and Ols-son, R. K.: Warm tropical sea surface temperatures in the Late Cretaceous and Eocene epochs, *Nature*, 413, 481–487, 2001. 1231
- Pearson, P. N., van Dongen, B. E., Nicholas, C. J., Pancost, R. D., Schouten, S., Singano, J. M., and Wade, B. S.: Stable warm tropical climate through the Eocene epoch, *Geology*, 35, 211–214, 2007. 1236
- Pearson, P. N., Foster, G. L., and Wade, B. S.: Atmospheric carbon dioxide through the Eocene-Oligocene climate transition, *Nature*, 461, 1110–1113, 2009. 1231
- Rathmann, S. and Kuhnert, H.: Carbonate ion effect on Mg/Ca, Sr/Ca and stable isotopes on the benthic foraminifera *Oridorsalis umbonatus* off Namibia, *Mar. Micropaleontol.*, 66, 120–133, 2008. 1238
- Rathmann, S., Hess, S., Kuhnert, H., and Mulitza, S.: Mg/Ca ratios of the benthic foraminifera *Oridorsalis umbonatus* obtained by laser ablation from core top sediments: Relationship to bottom water temperatures, *Geochem. Geophys. Geosy.*, 5, Q12013, doi:10.1029/2004GC000808, 2004. 1238
- Roberts, C. D., LeGrande, A. N., and Tripati, A. K.: Climate sensitivity to Arctic seaway restriction during the early Paleogene, *Earth Planet. Sci. Lett.*, 286, 576–585, 2009. 1233, 1235, 1261
- Roeckner, E., Bauml, G., Bonaventura, L., Brokopf, R., Esch, M., Giorgetta, M., Hagemann, S., Kirchner, I., Kornblueh, L., Manzini, E., Rhodin, A., Schlese, U., Schulzweida, U., and Tompkins, A.: The atmospheric general circulation model ECHAM5, Tech. rep., Max Planck Institute for Meteorology, Hamburg, available at: <http://www.mpimet.mpg.de>, 2003. 1261
- Schmidt, G. A., Ruedy, R., Hansen, J. E., Aleinov, I., Bell, N., Bauer, M., Bauer, S., Cairns, B., Canuto, V., Cheng, Y., Genio, A. D., Faluvegi, G., Friend, A. D., Hall, T. M., Hu, Y., Kelley, M., Kiang, N. Y., Koch, D., Lacis, A. A., Lerner, J., Lo, K. K., Miller, R. L., Nazarenko, L., Oinas, V., Perlwitz, J. P., Perlwitz, J., Rind, D., Romanou, A., Russell, G. L., Sato, M., Shindell, D. T., Stone, P. H., Sun, S., Tausnev, N., Thresher, D., and Yao, M. S.: Present day atmospheric

## EoMIP

D. J. Lunt et al.

Title Page

Abstract

Introduction

Conclusions

References

Tables

Figures

◀

▶

◀

▶

Back

Close

Full Screen / Esc

Printer-friendly Version

Interactive Discussion



## EoMIP

D. J. Lunt et al.

Title Page

Abstract

Introduction

Conclusions

References

Tables

Figures

◀

▶

◀

▶

Back

Close

Full Screen / Esc

Printer-friendly Version

Interactive Discussion



simulations using GISS ModelE: Comparison to in-situ, satellite and reanalysis data, *J. Climate*, 19, 153–192, 2006. 1261

Seki, O., Foster, G. L., Schmidt, D. N., Mackenden, A., Kawamura, K., and Pancost, R. D.: Alkenone and boron-based Pliocene  $p\text{CO}_2$  records, *Earth Planet. Sci. Lett.*, 292, 201–211, 2010. 1231

Sewall, J. O., Sloan, L. C., Huber, M., and Wing, S.: Climate sensitivity to changes in land surface characteristics, *Global Planet. Change*, 26, 445–465, 2000. 1261

Sexton, P. F., Wilson, P. A., and Pearson, P. N.: Microstructural and geochemical perspectives on planktic foraminiferal preservation: Glassy versus Frosty, *Geochem. Geophys. Geosy.*, 7, Q12P19, doi:10.1029/2006GC001291, 2006. 1237

Shellito, C. J. and Sloan, L. C.: Reconstructing a lost Eocene paradise: Part I. Simulating the change in global floral distribution at the initial Eocene thermal maximum, *Global Planet. Change*, 50, 1–17, 2006. 1261

Sluijs, A., Schouten, S., Pagani, M., Woltering, M., Brinkhuis, H., Damsté, J. S., Dickens, G. R., Huber, B. T., Reichert, G. J., Stein, R., and L. J. Lourens, J. M., Pedentchouk, N., Backman, J., and Moran, K.: Subtropical Arctic Ocean temperatures during the Palaeocene/Eocene thermal maximum, *Nature*, 441, 610–613, 2006. 1239, 1244

Sluijs, A., Rohl, U., Schouten, S., Sangiorgi, H. J. B. F., Sinningh-Damste, J. S., and Brinkhuis, H.: Paleocene-early Eocene paleoenvironments with special emphasis on the Paleocene-Eocene thermal maximum (Lomonosov Ridge, Integrated Ocean Drilling Program Expedition 302), *Paleoceanography*, 23, PA1S11, doi:10.1029/2007PA001495, 2008. 1239

Storey, M., Duncan, R. A., and Swisher, C. C.: Paleocene-Eocene thermal maximum and the opening of the northeast Atlantic, *Science*, 316, 587–589, 2007. 1235

Tindall, J., Flecker, R., Valdes, P. J., Schmidt, D. N., Markwick, P., and Harris, J.: Modelling oxygen isotope distribution of ancient seawater using a coupled ocean-atmosphere GCM: implications for reconstructing early Eocene climate, *Earth Planet. Sci. Lett.*, 292, 265–273, 2010. 1234, 1237

Wilkinson, B. H. and Algeo, T. J.: Sedimentary carbonate record of calcium-magnesium cycling, *Am. J. Sci.*, 289, 1158–1194, 1989. 1238

Winguth, A., Shellito, C., Shields, C., and Winguth, C.: Climate Response at the Paleocene-Eocene thermal maximum to greenhouse gas forcing – a model study with CCSM3, *J. Climate*, 23, 2562–2584, 2010. 1233, 1234, 1261

## EoMIP

D. J. Lunt et al.

Title Page

Abstract

Introduction

Conclusions

References

Tables

Figures



Back

Close

Full Screen / Esc

Printer-friendly Version

Interactive Discussion



Winguth, A. M. E., Thomas, E., and Winguth, C.: Global decline in ocean ventilation, oxygenation, and productivity during the Paleocene-Eocene Thermal Maximum: Implications for the benthic extinction, *Geology*, 40, 263–266, doi:10.1130/G32529.1, 2012. 1233, 1234, 1235, 1261

5 Yeager, S. G., Shields, C. A., Large, W. G., and Hack, J. J.: The low-resolution CCSM3, *J. Climate*, 19, 2545–2566, 2006. 1261

Zachos, J., Stott, L. D., and Lohmann, K. C.: Evolution of early Cenozoic marine temperatures, *Paleoceanography*, 9, 353–387, 1994. 1237

10 Zachos, J. C., Dickens, G. R., and Zeebe, R. E.: An early Cenozoic perspective on greenhouse warming and carbon-cycle dynamics, *Nature*, 451, 279–283, 2008. 1236

## EoMIP

D. J. Lunt et al.

**Table 1.** Summary of model simulations in EoMIP. Some models have irregular grids in the atmosphere and/or ocean, or have spectral atmospheres. The atmospheric and ocean resolutions are given in number of gridboxes,  $X \times Y \times Z$  where  $X$  is the effective number of gridboxes in the zonal,  $Y$  in the meridional, and  $Z$  in the vertical. See the original references for more details.

Name	Eocene simulation reference	Model name and reference	Atmosphere resolution	Ocean resolution	
HadCM	Lunt et al. (2010)	HadCM3L, Cox et al. (2001)	96 × 73 × 19	96 × 73 × 20	
ECHAM	Heinemann et al. (2009)	ECHAM5/MPI-OM, Roeckner et al. (2003)	96 × 48 × 19	142 × 82 × 40	
CCSM_W	Winguth et al. (2010, 2012)	CCSM3, Collins et al. (2006); Yeager et al. (2006)	96 × 48 × 26	100 × 116 × 25	
CCSM_H	Liu et al. (2009); Huber and Caballero (2011)	CCSM3, Collins et al. (2006); Yeager et al. (2006)	96 × 48 × 26	100 × 122 × 25	
GISS	Roberts et al. (2009)	GISS ModelE-R, Schmidt et al. (2006)	72 × 45 × 20	72 × 45 × 13	
Name	Paleogeography	Sim. length (yr)	CO <sub>2</sub> levels	Vegetation	Aerosols
HadCM	Propriety	> 3400	×2, 4, 6	Homogenous shrubland	As control
ECHAM	Bice and Marotzke (2001)	2500	×2	Homogenous woody savanna	As control
CCSM_W	Sewall et al. (2000) with marginal sea parameterisation	1500	×4, 8, 16	Shellito and Sloan (2006)	As control
CCSM_H	Sewall et al. (2000)	1500	×2, 4, 8, 16	Shellito and Sloan (2006)	Reduced aerosol
GISS	Bice and Marotzke (2001)	2000	×2	Sewall et al. (2000)	As control

Title Page

Abstract

Introduction

Conclusions

References

Tables

Figures



Back

Close

Full Screen / Esc

Printer-friendly Version

Interactive Discussion



## EoMIP

D. J. Lunt et al.

**Table 2.** Global mean temperatures and model mean-error scores for each simulation. Scores are calculated based on the SST ( $\sigma_{\text{sst}}$ ) and land surface air temperature ( $\sigma_{\text{lat}}$ ) data. Definitions of the scores are given in Eq. (2). Rows in bold indicate the best (i.e., lowest  $\sigma$ ) CO<sub>2</sub> level for each model.

Model	CO <sub>2</sub>	⟨SST⟩	⟨LAT⟩	⟨GST⟩	$\sigma_{\text{sst}}$ (°C)	$\sigma_{\text{lat}}$ (°C)
HadCM	2x	21.45	11.71	18.54	7.1	15.5
	4x	24.19	16.20	21.95	4.1	11.4
	6x	26.25	19.80	24.56	<b>2.1</b>	<b>7.7</b>
ECHAM	2x	24.65	20.59	24.03	<b>5.1</b>	<b>9.7</b>
CCSM.W	4x	22.31	16.26	20.95	7.0	10.3
	8x	24.61	19.57	23.59	4.5	7.2
	16x	27.20	23.16	26.46	<b>1.6</b>	<b>3.7</b>
CCSM.H	2x	22.66	15.71	21.12	7.5	11.5
	4x	24.41	18.41	23.17	5.8	8.5
	8x	26.86	21.66	25.79	3.1	5.1
GISS	16x	30.14	26.30	29.47	<b>-0.4</b>	<b>0.4</b>
	4x	26.43	21.97	23.25	<b>3.3</b>	<b>6.9</b>

Title Page

Abstract

Introduction

Conclusions

References

Tables

Figures

◀

▶

◀

▶

Back

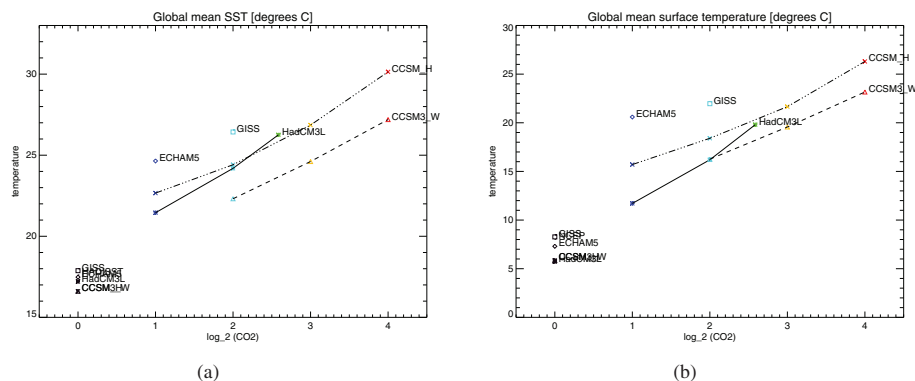
Close

Full Screen / Esc

Printer-friendly Version

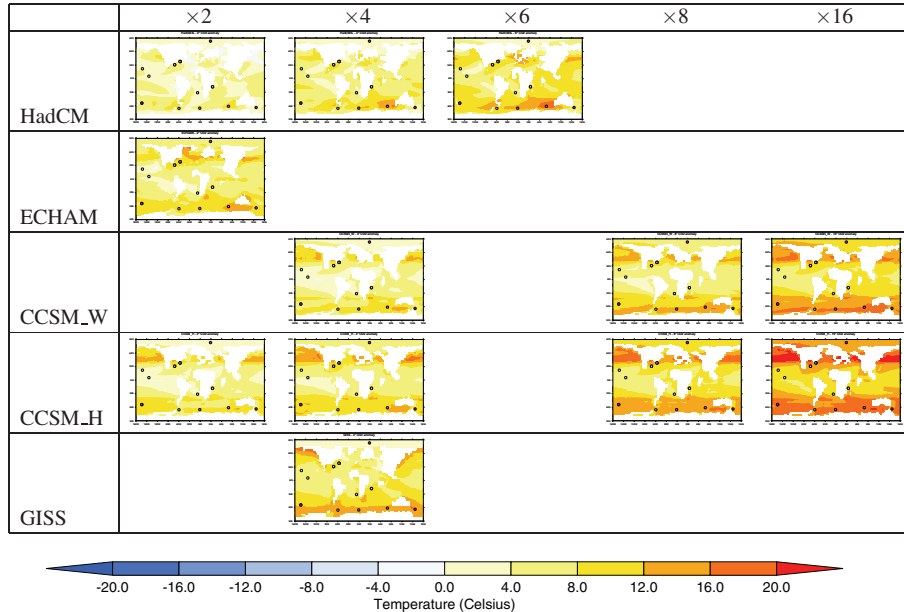
Interactive Discussion





**Fig. 1.** Global annual mean **(a)** SST (SST) and **(b)** continental 2 m air temperature (LAT), as a function of CO<sub>2</sub> for all simulations, and for observational datasets. The simulations at  $\times 1$  CO<sub>2</sub> are pre-industrial reference simulations.

[Title Page](#)
[Abstract](#)
[Introduction](#)
[Conclusions](#)
[References](#)
[Tables](#)
[Figures](#)
[⏪](#)
[⏩](#)
[◀](#)
[▶](#)
[Back](#)
[Close](#)
[Full Screen / Esc](#)
[Printer-friendly Version](#)
[Interactive Discussion](#)

**Fig. 2.** SST anomaly in the model simulations ( $SST_e^m - \overline{SST_p^m}$ ), as a function of model and fractional CO<sub>2</sub> increase from pre-industrial. Also shown for the proxies are  $SST_e^d - \overline{SST_p^d}$ .

Title Page

Abstract

Introduction

Conclusions

References

Tables

Figures

⏪

⏩

◀

▶

Back

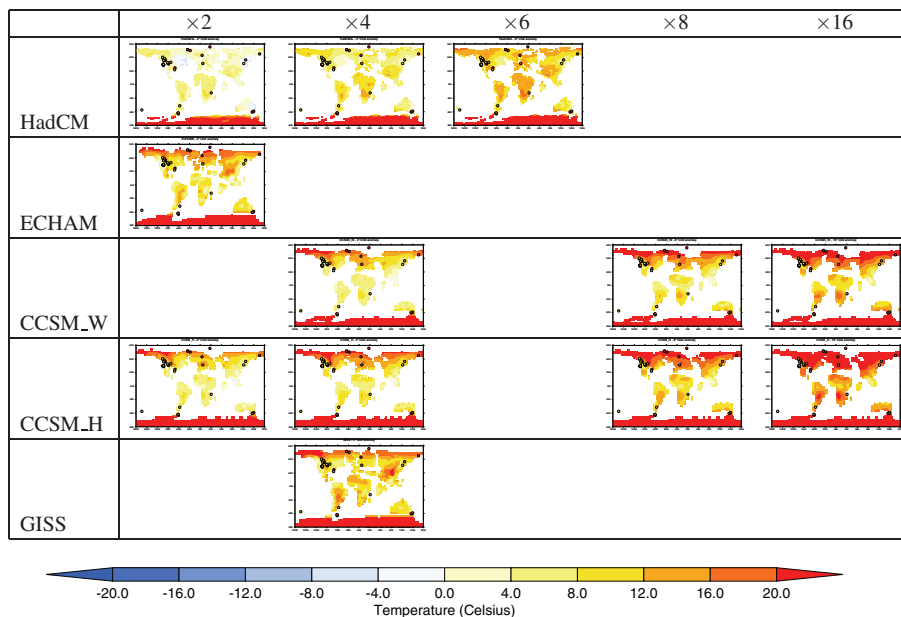
Close

Full Screen / Esc

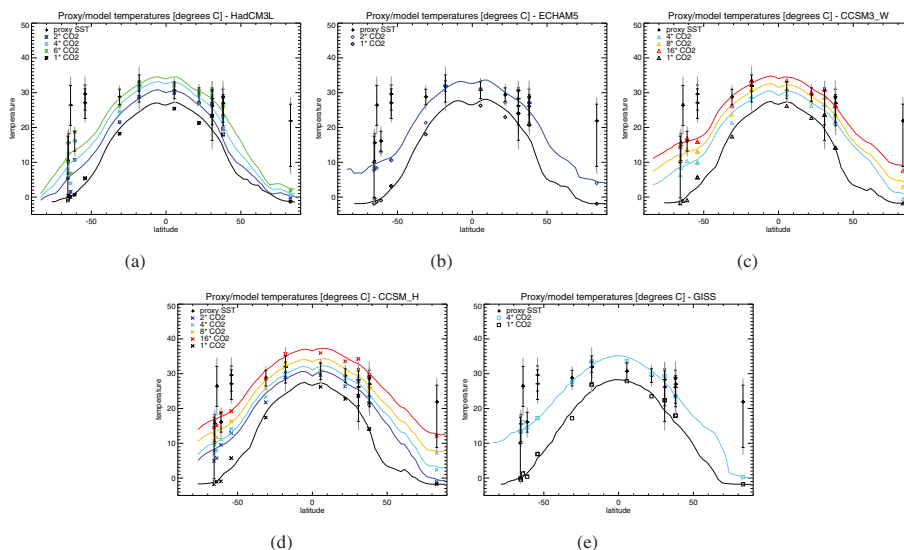
Printer-friendly Version

Interactive Discussion



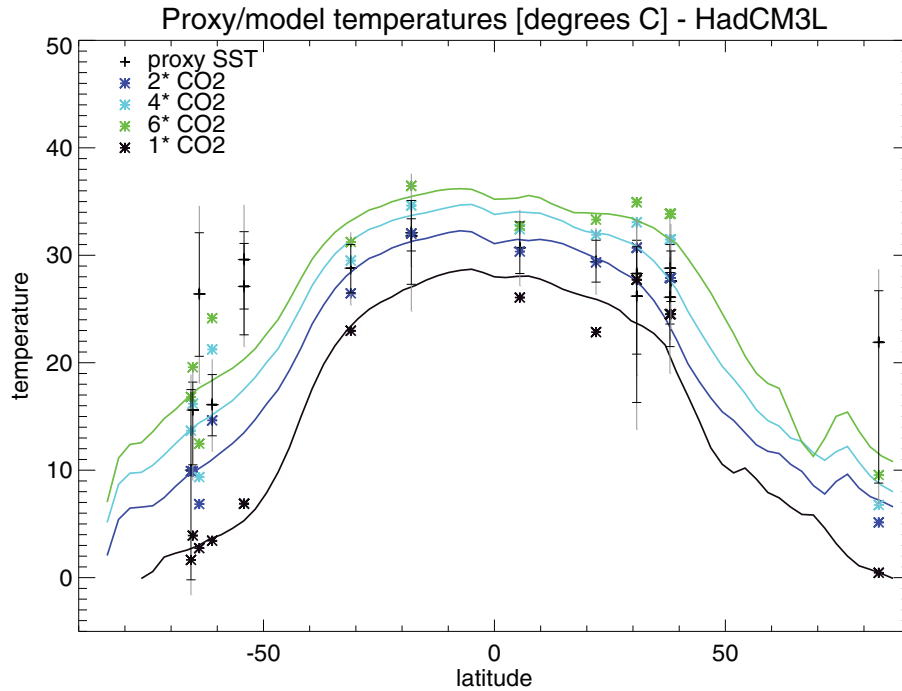


**Fig. 3.** Continental surface air temperature anomaly in the model simulations ( $\overline{\text{LAT}_e^m - \text{GAT}_p^m}$ ), as a function of model and fractional  $\text{CO}_2$  increase from pre-industrial. Also shown for the proxies are  $\overline{\text{LAT}_e^d - \text{GAT}_p^d}$ .



**Fig. 4.** Comparison of modelled SST with proxy-derived temperatures, SST vs. latitude. The simulations at  $\times 1$  CO<sub>2</sub> are pre-industrial reference simulations. For the model results, the continuous lines represent the zonal mean, and the symbols represent the modelled temperature at the same location (longitude, latitude) as the proxy data. For the proxy data, the symbols represent the proxy temperature, and the error bars represent the range. The range is made up of two components: calibration uncertainty (black bar) and temporal uncertainty (grey bar). See Sect. 3 and Supplementary Information for more details of the range calculations.

[Title Page](#)
[Abstract](#)
[Introduction](#)
[Conclusions](#)
[References](#)
[Tables](#)
[Figures](#)
[◀](#)
[▶](#)
[◀](#)
[▶](#)
[Back](#)
[Close](#)
[Full Screen / Esc](#)
[Printer-friendly Version](#)
[Interactive Discussion](#)

**Fig. 5.** As Fig. 4a, but the HadCM modelled zonal mean represents the warm month mean SST, as opposed to annual mean.

Title Page

Abstract

Introduction

Conclusions

References

Tables

Figures

◀

▶

◀

▶

Back

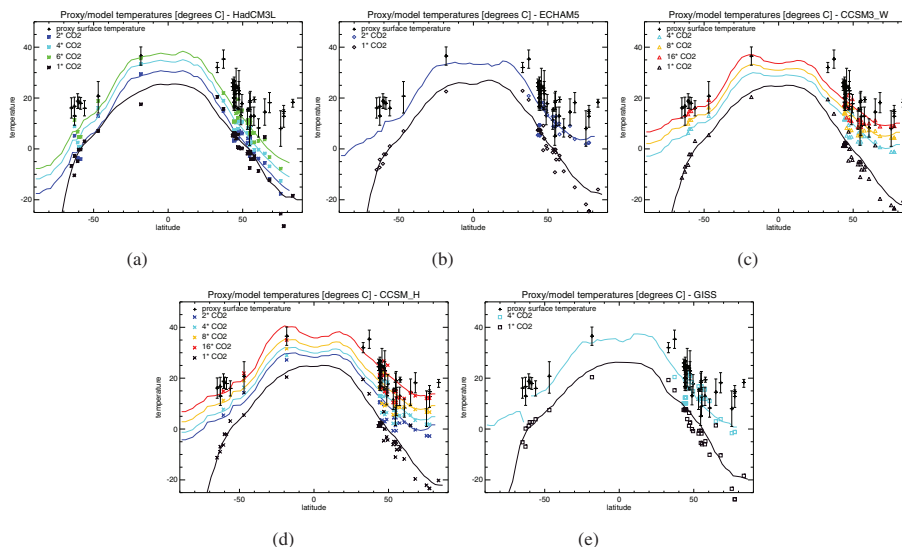
Close

Full Screen / Esc

Printer-friendly Version

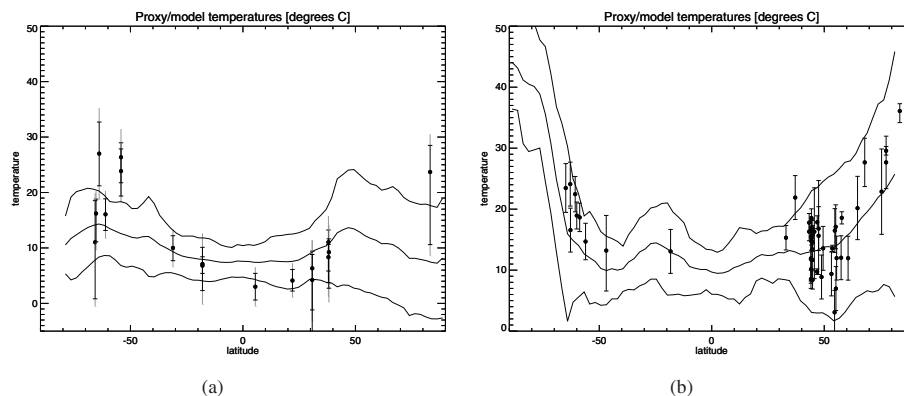
Interactive Discussion





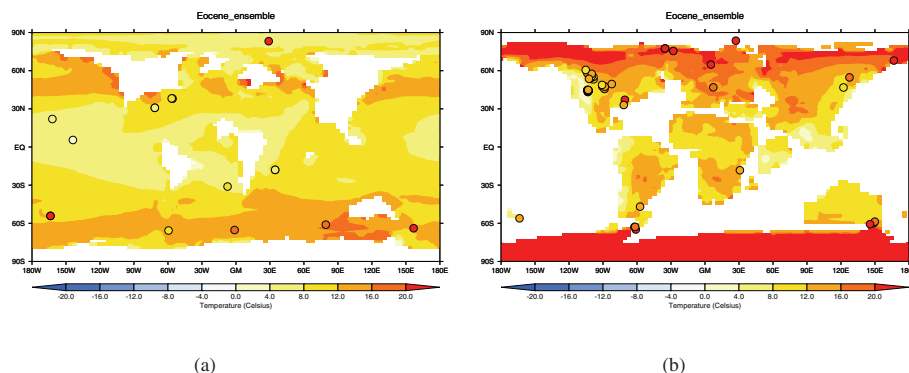
**Fig. 6.** Comparison of modelled SAT with proxy-derived temperatures, SAT vs. latitude. The simulations at  $\times 1$  CO<sub>2</sub> are pre-industrial reference simulations. For the model results, the continuous lines represent the zonal mean, and the symbols represent the modelled temperature at the same location (longitude, latitude) as the proxy data. For the proxy data, the symbols represent the proxy temperature, and the error bars represent the range, as given by Huber and Caballero (2011).

[Title Page](#)
[Abstract](#)
[Introduction](#)
[Conclusions](#)
[References](#)
[Tables](#)
[Figures](#)
[Back](#)
[Close](#)
[Full Screen / Esc](#)
[Printer-friendly Version](#)
[Interactive Discussion](#)

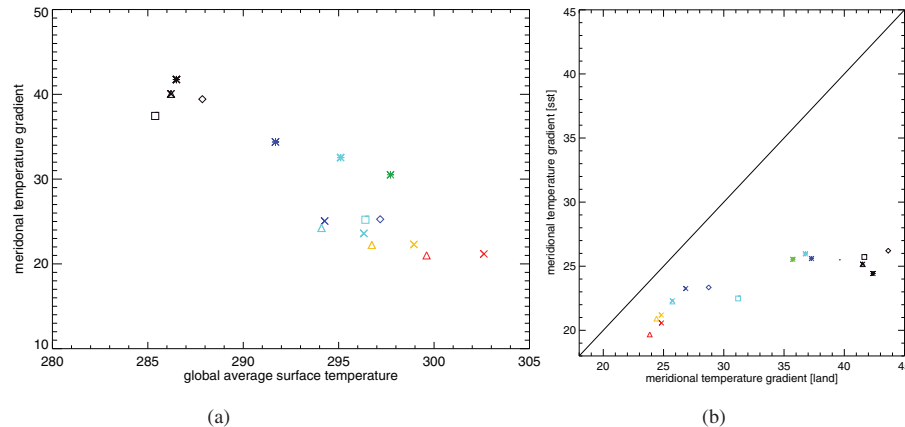
**Fig. 7.** Zonal ensemble mean model, and data, presented as an anomaly relative to present/pre-industrial. Light grey model lines indicate  $\pm 2$  standard deviations in the models. **(a)**  $[SST_e - SST_p]$ . **(b)**  $[LAT_e - GAT_p]$ . The ensemble consists of the best simulation from each model, as highlighted in bold in Table 2. Descriptions of the proxy error bars are given in the captions to Figs. 4 and 6.

[Title Page](#)
[Abstract](#)
[Introduction](#)
[Conclusions](#)
[References](#)
[Tables](#)
[Figures](#)
[⏪](#)
[⏩](#)
[◀](#)
[▶](#)
[Back](#)
[Close](#)
[Full Screen / Esc](#)
[Printer-friendly Version](#)
[Interactive Discussion](#)

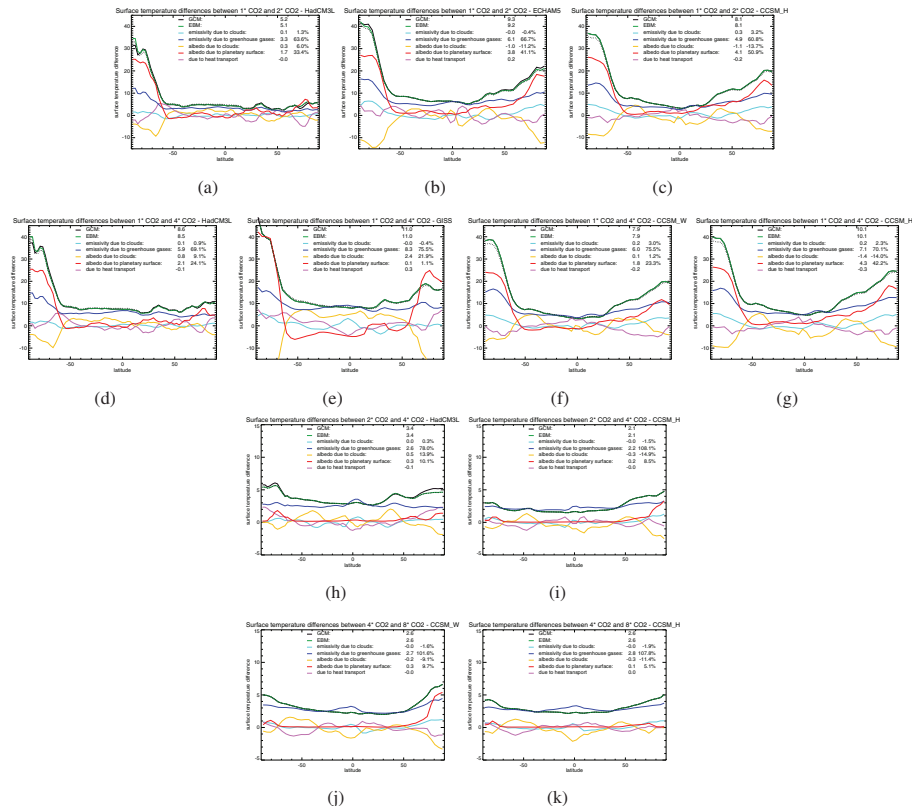



**Fig. 8.** Ensemble mean modelled Eocene warming, presented as an anomaly relative to present/pre-industrial. **(a)**  $[SST_e - SST_p]$ . **(b)**  $[LAT_e - GAT_p]$ . The ensemble consists of the best simulation from each model, as highlighted in bold in Table 2.

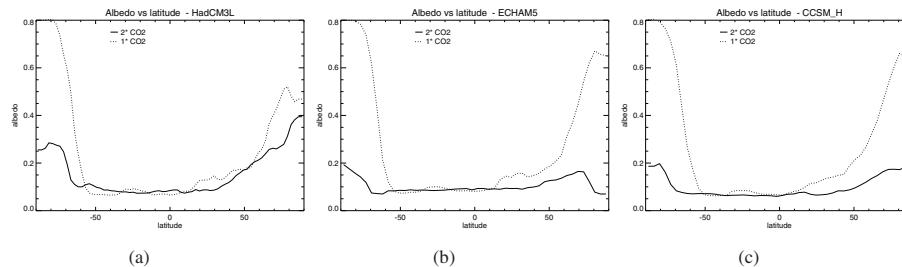
[Title Page](#)
[Abstract](#)
[Introduction](#)
[Conclusions](#)
[References](#)
[Tables](#)
[Figures](#)
[◀](#)
[▶](#)
[◀](#)
[▶](#)
[Back](#)
[Close](#)
[Full Screen / Esc](#)
[Printer-friendly Version](#)
[Interactive Discussion](#)

**Fig. 9.** (a) Meridional surface temperature gradient  $GST_{|\phi|>60} - GST_{|\phi|<30}$ , where  $|\phi|$  is the absolute value of the latitude in degrees, as a function of global average surface temperature,  $\langle GST \rangle$  for all the simulations presented in this paper. (b) Meridional surface temperature gradient over land/ocean,  $SST_{|\phi|>60} - SST_{|\phi|<30}$  vs.  $LAT_{|\phi|>60} - LAT_{|\phi|<30}$ . Symbols and colours correspond to those in Fig. 1.



**Fig. 10.** The zonal-mean surface temperature change under a range of CO<sub>2</sub> transitions, and energy balance analysis of the reasons for the changes. **(a–c)**  $\times 1$  to  $\times 2$  CO<sub>2</sub>, **(d–g)**  $\times 1$  to  $\times 4$  CO<sub>2</sub>, **(h, i)**  $\times 2$  to  $\times 4$  CO<sub>2</sub>, **(j, k)**  $\times 4$  to  $\times 8$  CO<sub>2</sub>. Note the difference in vertical scale in panels **(a–g)** compared with **(h–k)**.



**Fig. 11.** Zonal mean albedo in the  $\times 1$  and  $\times 2$  CO<sub>2</sub> simulations using the **(a)** HadCM, **(b)** ECHAM, and **(c)** CCSM\_H models.

[Title Page](#)[Abstract](#)[Introduction](#)[Conclusions](#)[References](#)[Tables](#)[Figures](#)[⏪](#)[⏩](#)[◀](#)[▶](#)[Back](#)[Close](#)[Full Screen / Esc](#)[Printer-friendly Version](#)[Interactive Discussion](#)